Metal-Dependent Self-Assembly of a Microbial Surfactant

Tate Owen,† Roger Pynn,‡ Boualem Hammouda,§ and Alison Butler*,†

Department of Chemistry & Biochemistry, University of California, Santa Barbara, California 93106-9510, Department of Physics, University of Indiana, Bloomington, Indiana 47405-4202, and National Institute of Standards and Technology, Building 235, Room E151, 100 Bureau Drive, Stop 8562, Gaithersburg, Maryland 20879-8562

Received March 7, 2007. In Final Form: May 8, 2007

Small-angle neutron scattering (SANS), cryogenic transmission electron microscopy (cryo-TEM), and dynamic light scattering (DLS) were used to study the metal-dependent phase behavior of microbially produced surfactants—marinobactins B, D, and E (M_B, M_D, and M_E). Marinobactins A−E are siderophores that facilitate Fe(III) acquisition by the source bacterium through the coordination of Fe(III) by the peptidic headgroup. All of the marinobactins have the same six amino acid headgroup but differ in the length and saturation of the monoalkyl fatty acid tail. Fe(III) coordinated to M_E (Fe(III)−M_E) was found to form micelles with a diameter of ∼3.5 nm that underwent a supramolecular transformation to produce a monodisperse population of vesicles with an average diameter ranging from ∼90 to 190 nm upon addition of Cd(II), Zn(II), or La(III). SANS profiles of the transition-metal-induced phase exhibit a Bragg peak at $Q_B \approx 0.11-0.12$ Å^{-1} and were fit to a SANS model for multilamellar vesicles that have an interbilayer repeat distance of $2\pi/Q_B \approx 5.6-5.0$ nm. Cryo-TEM images of the Zn(II)-induced phase reveals the presence of ∼100 nm diameter approximately spherical aggregates of uniform electron density. The temperature dependence of the Zn-(II)-induced transformation was also investigated as a function of the length and degree of unsaturation of the Fe-(III)−marinobactin fatty acid tail. The Cd(II)-, Zn(II)-, and La(III)-induced phase changes have features that are similar to those of the previously reported Fe(III)-induced micelle-to-vesicle transition, and this observation has opened questions regarding the role that Cd(II) and Zn(II) may play in bacterial iron uptake.

Introduction

Metal coordination by a surfactant is an attractive means of controlling the self-assembly of amphiphilic molecules. The coordination of a metal cation by a surfactant can change the ionic charge and/or molecular geometry of an amphiphile and thus can promote dramatic changes in the aggregate morphology. For example, whereas amphiphiles with a single fatty acid generally form micelles in solution, some synthetic single-tailed amphiphiles form vesicles upon coordination of transition-metal ions such as Ag(I),[1] Co(II),[2] and Fe(III).[3] Other single-tailed amphiphiles assemble as a bicontinuous "sponge" phase (L_3 phase) in the presence of Ca^{2+} and a co-surfactant,[4] and certain dual-tailed surfactants with imidazole-containing headgroups undergo a transformation from planar lamellae to closed multilamellar vesicles in the presence of Cu(II).[5,6] Even naturally occurring surfactants can exhibit metal-dependent phase changes. For example, cardiolipin, a biological phospholipid consisting of four fatty acid tails and two phosphate moieties, undergoes a transition from planar lamellae to a reversed hexagonal phase upon the addition of Ba^{2+}, Ca^{2+}, or Mg^{2+}.[7−9] The present work concerns the marinobactins, a suite of bacterial surfactants that undergo a micelle-to-vesicle transition in the presence of Fe-(III).[10,11]

Marinobactins A−E (M_A−M_E, Figure 1) are a suite of amphiphilic siderophores produced by the marine bacterium *Marinobacter* sp. DS40M6 to facilitate the acquisition of iron.[12] Siderophores are low-molecular-weight compounds secreted by bacteria that have large stability constants for Fe(III) and can solubilize colloidal iron oxide.[13,14] Each marinobactin comprises the same six amino acid peptidic headgroup that coordinates Fe(III) but differs in the identity of the fatty acid appendage (C_{12}−C_{16}) (Figure 1).

The critical micelle concentration (cmc) for both apo-M_E (i.e., M_E that is not coordinated to Fe(III)) and Fe(III)−M_E are relatively low at ca. 50 and ca. 75 μM, respectively.[10] Apo-M_E forms micelles above its cmc that decrease in size when apo-M_E coordinates 1 equiv of Fe(III).[11] In the presence of excess Fe(III) (i.e., Fe(III)/apo-M_E ratios of 1.1−3.0), the micelles rearrange to form large vesicles that are approximately 200 nm in diameter.[11] We have hypothesized that "excess" Fe(III) induces vesicle formation by bridging the terminal carboxylate moieties of two or three Fe(III)−M_E headgroups, drawing them closer together in an arrangement that favors a vesicular aggregate (Scheme 1).[11]

On the basis of the phase change that Fe(III)−M_E undergoes upon reaction with excess Fe(III), we have investigated the effects

* To whom correspondence should be addressed. E-mail: butler@chem.ucsb.edu.

† University of California.

‡ University of Indiana.

§ National Institute of Standards and Technology.

(1) Luo, X.; Miao, W.; Wu, S.; Liang, Y. *Langmuir* **2002**, *18*, 9611−9612.

(2) Luo, X.; Wu, S.; Liang, Y. *Chem. Commun.* **2002**, *5*, 492−493.

(3) Apostol, M.; Baret, P.; Serratrice, G.; Desbrières, J.; Putaux, J.-L.; Stébé, M.-J.; Expert, D.; Pierre, J.-L. *Angew. Chem.* **2005**, *117*, 2636−2638.

(4) Beck, R.; Abe, Y.; Terabayashi, T.; Hoffman, H. *J. Phys. Chem. B* **2002**, *106*, 3335−3338.

(5) van Esch, J. H.; Stols, A. L. H.; Nolte, R. J. M. *J. Chem. Soc., Chem. Commun.* **1990**, 1658−1660.

(6) Sommerdijk, N. A. J. M.; Booy, K. J.; Pistorius, A. M. A.; Feiters, M. C.; Nolte, R. J. M.; Zwanenburg, B. *Langmuir* **1999**, *15*, 7008−7013.

(7) Vasilenko, I.; De Kruijff, B.; Verkleij, A. J. *Biochim. Biophys. Acta* **1982**, *684*, 282−286.

(8) Vail, W. J.; Stollery, J. G. *Biochim. Biophys. Acta* **1979**, *551*, 74−84.

(9) Rand, R. P.; Sengupta, S. *Biochim. Biophys. Acta* **1971**, *255*, 484−492.

(10) Martinez, J. S.; Zhang, G. P.; Holt, P. D.; Jung, H.-T.; Carrano, C. J.; Haygood, M. G.; Butler, A. *Science* **2000**, *287*, 1245−1247.

(11) Owen, T.; Pynn, R.; Martinez, J. S.; Butler, A. *Langmuir* **2005**, *21*, 12109−12114.

(12) Martinez, J. S.; Carter-Franklin, J. N.; Mann, E. L.; Martin, J. D.; Haygood, M. G.; Butler, A. *Proc. Natl. Acad. Sci. U.S.A.* **2003**, *100*, 3754−3759.

(13) Dertz, E. A.; Raymond, K. N. In *Iron Transport in Bacteria*; Payne, S., Crosa, J., Eds.; ASM Press: Washington, DC, 2004; pp 5−17. Boukhalfa, H.; Crumbliss, A. L. *Biometals* **2002**, *15*, 325−339.

(14) Butler, A. *Science* **1998**, *281*, 207−210.

10.1021/la700671p CCC: $37.00
Published on Web 07/26/2007

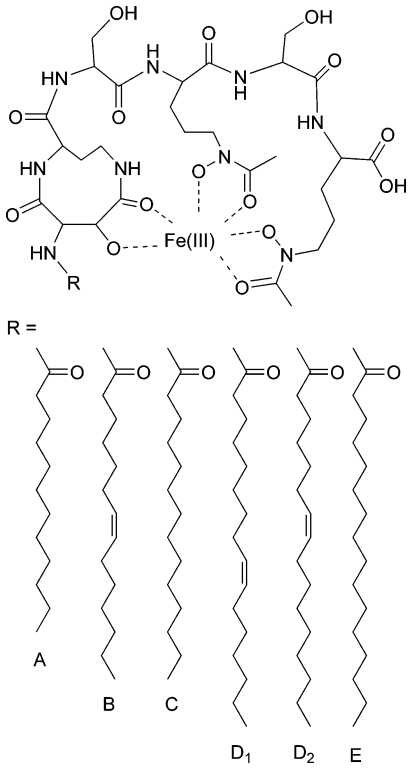

Figure 1. Structure of marinobactins A-E coordinated to Fe(III). The headgroup contains a carboxylic acid moiety that is anionic at neutral pH.

Scheme 1. The Headgroups of Fe(III)−M_E Bridged by Exogenous Fe(III) Could Pull the Headgroups Closer Together Resulting in a "Composite Surfactant" with a Lower Headgroup Area : Tail Volume Ratio That May Favor Vesicle Formation[36]

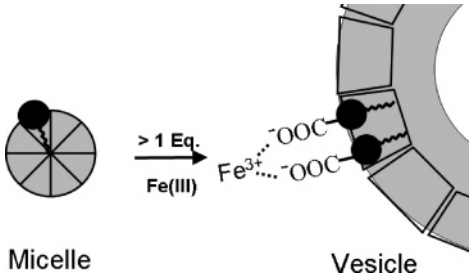

that a variety of other metal cations (Zn(II), Cd(II), La(III), etc.) have on the aggregate morphology of Fe(III)−M_E using dynamic light scattering (DLS), small-angle neutron scattering (SANS), and cryogenic transmission electron microscopy (cryo-TEM). We report that Cd(II), Zn(II), and La(III) induced the temperature-dependent formation of large multilamellar vesicles of Fe(III)−M_E.

Materials and Methods

Definitions. Fe(III)−M_B, Fe(III)−M_D, and Fe(III)−M_E refer to the iron complexes of marinobactins B, D, and E, respectively. Apo-M_B, apo-M_D, and apo-M_E indicate marinobactins B, D, and E, respectively, that are not coordinated to Fe(III).

Materials. Deuterium oxide, deuterium chloride, and sodium deuteroxide were purchased from Cambridge Isotope Laboratories, Inc. Triply deionized water (Barnstead NANOpure II) was used in all experiments. All other chemicals and organic solvents were purchased from EM Science. Apo-M_B, apo-M_D, and apo-M_E were obtained from a bacterial culture (*Marinobacter* species strain DS40M6) and purified as previously described.[10,11]

Sample Preparation. D_2O was used as a solvent in place of H_2O to maximize the neutron scattering contrast between Fe(III)−M_B, Fe(III)−M_D, or Fe(III)−M_E and the solvent and to obtain the optimum signal for SANS measurements. All samples analyzed by cryo-TEM, DLS, and SANS consisted of 1.4 mM Fe(III)−M_B, Fe(III)−M_D, or Fe(III)−M_E in D_2O at pD 6.0. Fe(III)−M_B, Fe(III)−M_D, and Fe(III)−M_E were prepared by adding 0.9 equiv of Fe(III) to apo-M_B, apo-M_D, and apo-M_E, respectively. The concentration of apo-M_E was determined by spectrophotometric titration at 400 nm (i.e., λ_{max} of Fe(III)−M_E) with a standardized stock solution of Fe(III). Fe(III) was added to apo-M_B, apo-M_D, or apo-M_E from a standardized stock solution of 0.073 M $FeCl_3$ in 0.05 M DCl in D_2O. The concentration of the Fe(III) stock solution was determined spectrophotometrically with 1,10-phenanthroline at pH 4 after the addition of hydroxylamine: $Fe(phen)_3^{2+}$ λ_{max} 510 nm, ϵ 11 000 M^{-1} cm^{-1}.[15] The metal cations were added to Fe(III)−M_B, Fe(III)−M_D, or Fe(III)−M_E solutions at 25 °C from stock solutions of 1 M $ZnCl_2$, $CdCl_2$, $CaCl_2$, or $La(NO_3)_3$ in 0.05 M DCl in 99.9% D_2O and then equilibrated at the appropriate temperature for at least 3 days prior to cryo-TEM, DLS, and SANS experiments. pD adjustments were accomplished with NaOD and DCl. The standard correction of pD = pH + 0.4 was applied for all titrations in D_2O.

SANS Instrumentation. SANS experiments were conducted on the 30 m NG3 SANS station at the NIST Center for Neutron Research (NCNR) in Gaithersburg, Maryland. Two different instrument configurations were used. In the first configuration, SANS data were acquired using an average neutron wavelength of 6 Å at sample-to-detector distances of 1.3 and 13.2 m. Combining SANS data taken at 1.3 and 13.2 m sample-to-detector distances allowed neutron wavevector transfers (Q) in the range of 0.003 $Å^{-1} < Q < 0.4$ $Å^{-1}$ to be accessed, where $Q = (4\pi/\lambda)\sin(\theta/2)$ and θ represents the neutron scattering angle. The second instrument configuration employed an average neutron wavelength of 8.4 Å and combining SANS data from three sample-to-detector distances (1.3, 5.5, and 13.2 m) allowed in the Q range of 0.001 $Å^{-1} < Q < 0.3$ $Å^{-1}$ to be accessed.

SANS samples were loaded into quartz cuvettes (volume = 1.6 mL) with a path length of 5 mm and a window area of 3.2 cm^2. The 2-D raw SANS intensity data were corrected for background as well as scattering from the cuvette containing the sample and were put on an absolute scale by a standard procedure that estimates the neutron flux at the sample.[16] The data were then circularly averaged to produce 1-D SANS profiles of scattered neutron intensity, $I(Q)$, versus neutron wavevector transfer, Q.

Scattering Models. Several models were investigated to describe the SANS data. Models for micelles and multilamellar vesicles were found to give the best fits and are individually described below. In some cases, a linear combination of models for micelles and multilamellar vesicles was used. Least-squares fits to the SANS profiles were performed using Igor Pro (version 4.0.6.1) and software provided by the NCNR. The scattering models were convolved with the instrumental resolution (resulting from the spread in λ, instrument geometry, etc.) before being fit to experimental data. The level of incoherent neutron scattering was an adjustable parameter in the fits that was determined by the data because sufficiently high values of wavevector transfer were measured. Absolute levels of incoherent background were as expected for samples in D_2O. The difference in the neutron scattering-length density (SLD) between Fe(III)−M_B, Fe(III)−M_D, or Fe(III)−M_E and solvent (D_2O) was calculated to be 4.12×10^{-6} $Å^{-2}$ using the neutron scattering-length density calculator available on the NCNR website.

Micelle Scattering Model. Scattering from micelles was fitted with a form factor for a spherical particle whose average radius was assumed to be polydisperse according to a Shultz distribution (Figure 2).[17,18] Because there was negligible correlation between particle positions at the low surfactant concentrations used in this work,

(15) Marczenko, Z. *Separation and Spectrophotometric Determination of Elements*; Ellis Horwood: Chichester, U.K., 1986; Chapter 27.
(16) Glinka, C. J.; Barker, J. G.; Hammounda, B.; Krueger, S.; Moyer, J. J.; Orts, W. J. *J. Appl. Crystallogr.* **1998**, *31*, 430−445.
(17) Griffith, W. L.; Triolo, R.; Compere, A. L. *Phys. Rev. A* **1987**, *35*, 2200−2206.

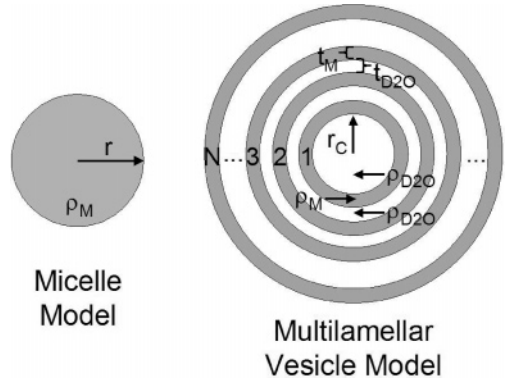

Figure 2. SANS models for a micelle and a multilamellar vesicle. The micelle radius, r is allowed to be polydisperse according to a Shultz distribution and the micelle has the scattering length density (SLD) of Fe(III)-marinobactin (ρ_M). The multilamellar vesicle has N bilayers wrapped around a core that has the SLD of D_2O (ρ_{D2O}) and the core radius, r_C, is polydisperse according to a Shultz distribution. Concentric shells of thickness t_M have the SLD of Fe-(III)-marinobactin (ρ_M) and represent lipid bilayers. Between lipid bilayer shells are layers of thickness t_{D2O} and have the SLD of ρ_{D2O}.

scattering from micelles was completely described by a form factor (i.e., the structure factor is set to unity for all scattering vectors). The micelle model is described in detail on the NCNR website (Supporting Information).

Multilamellar Vesicle Scattering Model. Scattering from the large ~100 nm Cd(II)- and Zn(II)-induced aggregates was analyzed using a scattering model for multilamellar vesicles. The multilamellar vesicles are represented by a spherical particle consisting of a core with the scattering length density (SLD) of the solvent (ρ_{D_2O}) and N concentric shells of thickness t_M that had the SLD of Fe(III)−marinobactin (ρ_M). Layers of thickness t_{D_2O} that had the SLD of ρ_{D_2O} are located between concentric shells of thickness t_M (Figure 2).

The form factor for such a multishelled particle with N shells is

$$F_N(q, a_i(r), b_i(r)) = \sum_{i=0}^{N}\left\{\left((\rho_{D_2O} - \rho_M)\frac{4\pi}{3}(a_i(r))^3 F(qa_i(r))\right) + \left((\rho_M - \rho_{D_2O})\frac{4\pi}{3}(b_i(r))^3 F(qb_i(r))\right)\right\} \quad (1)$$

where $F(qa_i(r))$ and $F(qb_i(r))$ are the form factors for spheres of radii $a_i(r)$ and $b_i(r)$, respectively.

$$F(qa_i(r)) = \frac{3\sin(qa_i(r)) - qa_i(r)\cos(qa_i(r))}{(qa_i(r))^3} \quad (2)$$

$$F(qb_i(r)) = \frac{3\sin(qb_i(r)) - qb_i(r)\cos(qb_i(r))}{(qb_i(r))^3} \quad (3)$$

and

$$a_i(r) = r + it_M + it_{D_20} \quad (4)$$

$$b_i(r) = r + (i+1)t_M + it_{D_20} \quad (5)$$

Polydispersity in the core radius is added by squaring the multilamellar vesicle form factor $F_N(q, b_i(r), a_i(r))$, multiplying it by the Shultz distribution function $G(r)$, and integrating over the core radius

$$I(q) = \frac{\phi}{\mathrm{Vol}}\int_0^\infty G(r)\, F_N{}^2(q, a_i(r), b_i(r))\, \mathrm{d}r + bkg \quad (6)$$

where bkg is a constant that represents the incoherent scattering intensity and ϕ represents the volume fraction of multilamellar vesicles. ϕ is normalized to the multilamellar vesicle volume, termed Vol. Vol is corrected for polydispersity by multiplying the equation for the volume of a sphere of radius $r + Nt_M + (N-1)t_{D_2O}$ by the Shultz distribution function $G(r)$ and integrating over the core radius r.

$$\mathrm{Vol} = \int_0^\infty G(r)\left[\frac{4\pi}{3}\{r + N(t_M + t_{D_2O})\}^3\right]\mathrm{d}r \quad (7)$$

The Shultz distribution function is defined as follows

$$G(r) = (Z+1)^{(Z+1)}\left(\frac{r}{\bar{r}}\right)^Z \frac{\exp\left(-(Z+1)\left(\frac{r}{\bar{r}}\right)\right)}{\bar{r}\Gamma(Z+1)} \quad (8)$$

where $\bar{r}$ is the average core radius, $\Gamma(Z+1)$ is the gamma function, and Z is related to the polydispersity, σ, of the core radius according to the expression.

$$\sigma^2 = \left(\frac{\overline{r^2}}{\bar{r}^2} - 1\right) = \frac{1}{Z+1} \quad (9)$$

In one case, SANS data were analyzed using a multilamellar vesicle model that describes three populations of multilamellar vesicles. Each vesicle population differs in the number of lipid bilayers and the volume fraction. (All other vesicle parameters are identical.) The number of bilayers in each vesicle population is restricted to be consecutive numbers (i.e., vesicle populations 1, 2, and 3 have N, N + 1, and $N + 2$ bilayers, respectively, where N is any integer). The expression for the simulated SANS profile of such a mixed population of vesicles is

$$I(q) = \sum_{X=0}^{2}\left\{\frac{\phi_{N+X}}{\mathrm{Vol}_{N+X}}\int_0^\infty G(r)F_{N+X}{}^2(q, a_i(r), b_i(r))\,\mathrm{d}r\right\} + bkg \quad (10)$$

where $F_{N+X}(q, b_i(r), a_i(r))$ is the form factor for a multilamellar vesicle with $N + X$ bilayers (i.e., eq 1 with $N + X$ bilayers instead of N bilayers) and ϕ_{N+X} represents the volume fraction of vesicles with $N + X$ bilayers. ϕ_{N+X} is normalized by the volume of a vesicle with $N + X$ bilayers, termed Vol_{N+X}. Vol_{N+X} is corrected for polydispersity in the vesicle core diameter in the same manner as Vol in eq 7 except that the vesicle has $N + X$ bilayers instead of N bilayers.

Dynamic Light Scattering. DLS measurements were carried out on a Brookhaven BI-200SM goniometer with an AT9000 digital autocorrelator equipped with a Melles Griot 30 mW HeNe laser (λ = 633 nm). The correlation function itself was calculated between delay times of 5 and 1×10^5 μs and was analyzed by the method of cumulants.[19] Measurements were taken in 12 mm round glass cells in a temperature-controlled toluene bath with the detector set perpendicular (90°) to the incident laser beam. The diffusion coefficient was calculated using values of the viscosity and the refractive index of D_2O at the appropriate temperature, and a hydrodynamic diameter was calculated by assuming that the particle was spherical. Measurements of particle size by DLS were repeated several times to obtain a standard deviation of ~5 nm for the hydrodynamic diameter. The DLS instrument used for these experiments cannot be used to characterize particles with diameters of less than ~7 nm and thus cannot be used to size the micelles encountered in this work.

Cryogenic Transmission Electron Microscopy. Solutions of 1.4 mM Fe(III)−M_E containing 3.5 mM Zn(II) (in D_2O, pD 6.0) were equilibrated at 37 °C for 72 h prior to being prepared for

(18) DeGiorgio, V.; Corti, M. *Physics of Amphiphiles: Micelles, Vesicles, and Microemulsions*; North-Holland: Amsterdam, 1983; p 69.

(19) Koppel, D. E. *J. Chem. Phys.* **1972**, *57*, 4814−4820.

cryo-TEM.[20] The surfactant−D_2O mixture was spread as a thin (<1 μm) film on a lacey carbon grid (made by Ted Pella of Redding, CA) at 37 °C in a controlled-environment vitrification system (CEVS).[21] The samples were plunged onto a mixture of liquid ethane and liquid propane cooled by liquid nitrogen. After vitrification, samples were transferred to a GATAN (Pleasanton, CA) cold stage and imaged at 100 kV using a JEOL 100CXII transmission electron microscope. Images were recorded under low electron doses to prevent sample deterioration and were recorded with a CCD camera.

Results

Zinc(II)-Induced Phase Transition with Fe(III)−M_E. *Dynamic Light Scattering.* Fe(III)−M_E forms a micellar phase when present in aqueous solution at concentrations exceeding its cmc (ca. 75 μM in 100 mM KCl, 50 mM tris buffer, pH 8.0).[10,11,22] In the presence of Zn(II), Fe(III)−M_E undergoes a phase change at 37 °C. At this temperature, solutions of Fe(III)−M_E (1.4 mM, pD 6.0) containing >1.8 mM Zn(II) (i.e., >1 equiv of Zn(II) per Fe(III)−M_E) become turbid within 24 h. At higher Zn(II) concentrations (i.e., 3.5 and 4.4 mM, which are approximately 2.5:1 and 3:1 molar ratios of Zn(II)/Fe(III)−M_E, respectively), dynamic light scattering (DLS) measurements reveal the presence of a monodisperse (polydispersity <0.2) population of large, non-micellar particles. Although the polydispersity is low for each sample, the average particle diameter obtained from at least 10 sample preparations of the same composition (i.e., 1.4 mM Fe(III)−M_E, 3.5 mM Zn(II), pD 6.0, 37 °C) varies between 90 and 170 nm. After 48 h of equilibration, the turbidity and particle size at 3.5 and 4.4 mM Zn(II) remain stable for several months as monitored by DLS. Adding >4.4 mM Zn(II) (i.e., >3:1 Zn(II)/Fe(III)−M_E) results in the formation of an orange precipitate.[23] In contrast, other cations (i.e., Na^+, Ba^{2+}, and Ca^{2+}) do not induce a phase change at 8, 25, or 37 °C as monitored by DLS and SANS (Supporting Information and Table S-1).

In contrast to the Zn(II)-induced phase change for Fe(III)−M_E that occurred at 37 °C, at temperatures below 25 °C, the addition of up to 4.4 mM Zn(II) (i.e., 3:1 Zn(II)/Fe(III)−M_E) does not produce a change in the turbidity of Fe(III)−M_E solutions, as measured by DLS, suggesting that the Zn(II)-induced particles do not form. Nevertheless, once the Zn(II)-induced particles have formed at 37 °C, lowering the temperature to 25 or 8 °C does not reverse the transition, and the ∼90−170 nm diameter particles persist as monitored by DLS. However, these particles can be dissolved by the addition 2 mM EDTA;[24] that is, the solution turbidity of the Zn(II)-induced particles that were formed under conditions of 1.4 mM Fe(III)−M_E, 3.5 mM Zn(II) at pD 6.0, 37 °C returns to the baseline value of Fe(III)−M_E in the absence of Zn(II), as monitored by DLS. Thus, EDTA coordinates Zn(II), reducing the concentration that is required to effect vesicle formation. (See the SANS section below.)

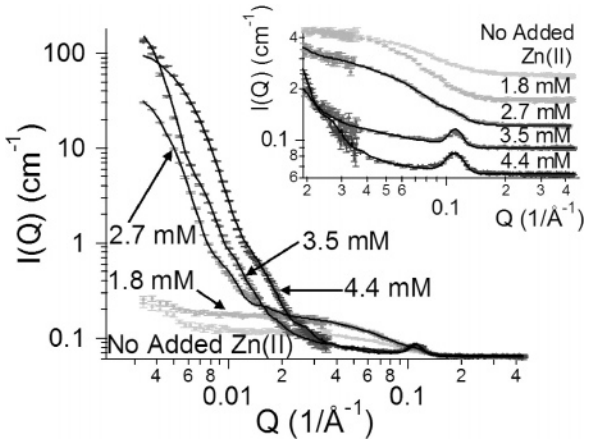

Figure 3. SANS profiles for 1.4 mM Fe(III)−M_E with increasing concentrations of Zn(II), pD 6.0, 37 °C. Zn(II) concentration is indicated. Solid Lines are the fits to the SANS model that included micelles and multilamellar vesicles. Inset: SANS profiles offset on *y*-axis for clarity.

Small-Angle Neutron Scattering. The Zn(II)-induced transition was also studied using SANS. SANS measurements reveal that Fe(III)−M_E solutions with no added Zn(II) or slightly more than 1 equiv of Zn(II) (i.e., 1.8 mM Zn(II) and 1.4 mM Fe(III)−M_E) consist primarily of micelles (Figure 3), which is consistent with DLS measurements. Furthermore, the fitted micellar diameter is greater in the presence of 1.8 mM Zn(II) relative to the case with no added Zn(II) (∼4.7 and ∼3.5 nm, respectively, also see Supporting Information, Table S-1). When the Zn(II) concentration is increased (i.e., 2.7 mM−4.4 mM Zn(II), which is *ca.* 2−3 equiv Zn(II) to Fe(III)−M_E with equilibration at 37 °C for 3 days) the SANS profiles show a decrease in the high Q scattered intensity from the micelles and a large increase in the low-Q scattered intensity, which results from a population of much larger aggregates (∼ 100 nm). SANS profiles with 3.5 mM and 4.4 mM Zn(II) (i.e., *ca.* 2.5 and 3.0 molar equiv of Zn(II) to Fe(III)−M_E) also exhibit a Bragg-type peak at $Q_B \sim 0.11$ Å^{-1} (Figure 3 inset), suggesting the Zn(II)-induced aggregates have an internal periodic structure with a periodicity of $2\pi/Q_B \sim 56$ Å.

The SANS data for the Zn(II)-induced phase were fit by a linear combination of a model for polydisperse spheres (i.e., micelles, Figure 2) and a model for core−shell particles with multiple shells (i.e., multilamellar vesicles, Figure 2). A similar quality of fit to the SANS data (e.g., χ^2 value) could be obtained by replacing the multilamellar vesicle model with a model for stacks of discs (i.e., stacked lamellae). However, the multilamellar vesicle model was deemed more appropriate on the basis of the observation of spherical particles by cryo-TEM. (See below.) To fit the SANS data for the Zn(II)-induced phase, the micelle diameter and polydispersity were constrained to that obtained from SANS measurements of Fe(III)−M_E micelles at 1.8 mM Zn(II) (Figure 3), and the vesicle bilayer thickness and interbilayer thickness were fixed equal to each other so that their sum equaled the periodicity implied by the Bragg peak at $Q_B \approx 0.11$ Å^{-1} ($2\pi/Q_B \approx 5.6$ nm = interbilayer thickness + bilayer thickness). The model was then fit to the SANS data by minimizing χ^2 with respect to four parameters (i.e., micelle volume fraction, vesicle volume fraction, vesicle core diameter, and vesicle core poly-

(20) (a) Jung, H.-T.; Coldren, B.; Zasadzinski, J. A.; Iampietro, D.; Kaler, E. W. *Proc. Natl. Acad. Sci. U.S.A.* **2001**, *98*, 1353−1357. (b) Jung, H.-T.; Lee, S. Y.; Coldren, B.; Zasadzinski, J. A.; Kaler, E. W. *Proc. Natl. Acad. Sci. U.S.A.* **2002**, *99*, 15318−15322.

(21) Bellare, J. R.; Davis, H. T.; Scriven, L. E.; Talmon, Y. *J. Electron Microsc. Tech.* **1988**, *10*, 87.

(22) Zhang, G. P. Ph.D. Dissertation. University of California, Santa Barbara, CA, 1999.

(23) After the addition of 2.7−4.4 mM Zn(II) to 1.4 mM Fe(III)−M_E (pD 6.0, 37 °C), a small quantity of orange precipitate forms, accompanied by an approximate 10% decrease in the absorbance at 400 nm (i.e., the λ_{max} of the Fe(III)−M_E complex). The decrease in absorbance at 400 nm is consistent with the precipitation of Fe(III)−M_E. It is not likely that Zn(II) displaces Fe(III) from the Fe(III)−M_E complex, given that these types of hydroxamate siderophores have a greater affinity for Fe(III) than Zn(II) and other divalent transition-metal ions.

(24) The addition of 2 mM EDTA to the Zn(II)-induced vesicles formed under conditions of 1.4 mM Fe(III)−M_E, 3.5 mM Zn(II), 2 mM EDTA, pD 6.0 at 37 °C is expected to lower the concentration of "available" Zn(II) (e.g., Zn(II) that is not coordinated to EDTA) to ca. 1.5 mM. This Zn(II) concentration is too low to stabilize the Zn(II)-induced Fe(III)−M_E vesicles. The addition of a near-stoichiometric concentration of EDTA (i.e., 3 mM EDTA or 3.5 mM Zn(II)) competes effectively with apo M_E for coordination of Fe(III) at the pH of these experiments (pD 6). Apo M_E does not undergo the micelle-to-vesicle transition. Thus, higher concentrations of EDTA also dissolve the Zn(II)-induced particles by coordination of both Zn(II) and Fe(III).

Table 1. Micelle and Vesicle Parameters for Fe(III)−M_E with Zn(II) or Cd(II)[a]

SANS fit parameters		Zn(II) 2.7 mM	Zn(II) 3.5 mM	Zn(II) 4.4 mM	Cd(II) 3.5 mM
micelle	volume fraction (±0.001%)	0.067	0.015	0.005	0.009
	diameter (±0.1 nm)[b]	4.7	4.7	4.7	4.7
	polydispersity (±0.01)[b]	0.23	0.23	0.23	0.23
multilamellar vesicles	vesicle diameter	121	181	77[c]	92
	core diameter (±0.6 nm)	17.3	12.6	10.2	16.6
	core polydispersity (±0.01)	1.00	0.90	1.00	0.90
	bilayer thickness[b]	2.8	2.8	2.8	2.7
	interbilayer thickness[b]	2.8	2.8	2.8	2.7
vesicle population no. 1	volume fraction (±0.001%)	0.018	0.087	0.057	0.135
	no. of bilayers	10	15	6	7
vesicle population no. 2	volume fraction (±0.001%)			0.007	
	no. of bilayers			7	
vesicle population no. 3	volume fraction (±0.001%)			0.035	
	no. of bilayers			8	
	χ^2	1.8	4.8	11.1	13.6

[a] Fe(III)−M_E (1.4 mM), pD 6.0, 37 °C. [b] Micelle diameter and polydispersity as well as vesicle bilayer thickness and interbilayer thickness are constrained as described in the text. [c] Diameter of vesicles with six bilayers.

dispersity) for different fixed values of the number of vesicle bilayers.

At Zn(II) concentrations of 2.7, 3.5, and 4.4 mM Zn(II) (with 1.4 mM Fe(III)−M_E), the best fit is obtained with a multilamellar vesicle whose solvent-filled core has a much smaller average diameter than the entire vesicle (<15% of the entire vesicle diameter, Table 1), suggesting that the vesicles may have bilayers with ranges of curvature that extend nearly to the center of the vesicle.[25] The SANS data at 4.4 mM Zn(II) is actually fit best by a model that describes a mixture of vesicles with six, seven, and eight bilayers (i.e., a linear combination of three multilamellar vesicle models; see Supporting Information, Figure S-2 and Table S-2) and suggests that the vesicles at 4.4 mM Zn(II) may be more polydisperse than those at 2.7 and 3.5 mM Zn(II). The SANS profile of the Cd(II)-induced particles (Figure 6) was also fit to the micelle-plus-multilamellar-vesicle SANS model (Table 1), and the results are discussed below.

Cryogenic Transmission Electron Microscopy. Visualization of the Zn(II)-induced Fe(III)−M_E particles (3.5 mM Zn(II)/1.4 mM Fe(III)−M_E) by cryo-TEM revealed a population of approximately circular aggregates (~100 nm diameter) that appeared to be solid (Figure 4). Tilting the cryo-TEM sample from −45 to 45° (with 0° representing the sample surface normal oriented parallel to the electron beam) did not change the observed diameter of the Zn(II)-induced particles, suggesting that the particles are spherical (data not shown). The cryo-TEM images of the Zn(II)-induced particles (Figure 4) do not show a hollow interior that is typical of many multilamellar vesicles. However, if the interior contains a sufficient number of bilayers, then the core could appear solid by cryo-TEM. In addition, the cryo-TEM image did not show resolved bilayers in each putative

(25) The considerable polydispersity in core diameter (0.90−1.00, Table 1) means that a significant fraction of the vesicles in the model have a core diameter of less than 1 nm, in which case the innermost bilayers would have an unrealistically high curvature. The large polydispersity in core diameter may be an artifact that results from parameters that are unaccounted for in the model such as the presence of non-spherical vesicles or fluctuations in the distance between bilayers.

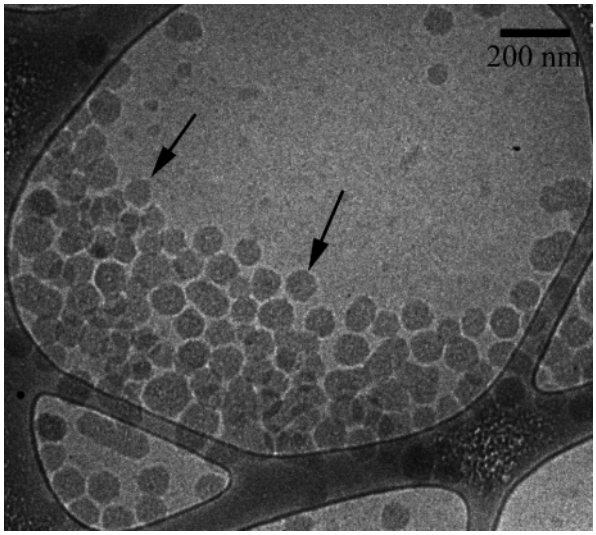

Figure 4. Cryoelectron micrograph of 1.4 mM Fe(III)−M_E with 3.5 mM $ZnCl_2$, pD 6.0, (37 °C prior to vitrifying sample). Scale bar represents 200 nm. Arrows indicate representative particles.

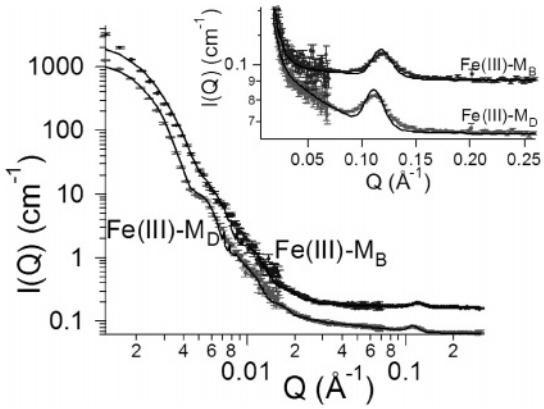

Figure 5. SANS profiles for 1.4 mM Fe(III)−M_B and Fe(III)−M_D with 0.5 mM and 3.5 mM $ZnCl_2$, respectively, pD 6.0, 25 °C. Solid lines are the fits to the multilamellar vesicle plus micelle model. Inset: SANS profiles are offset on the *y*-axis for clarity.

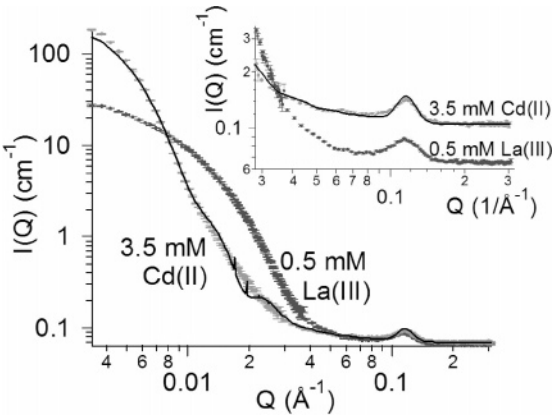

Figure 6. SANS profiles for 1.4 mM Fe(III)−M_E with 3.5 mM $CdCl_2$ and 0.5 mM $La(NO_3)_3$, pD 6.0, 37 °C. Solid line is the fit to the multilamellar vesicle plus micelles model for 3.5 mM Cd(II). Inset: SANS profiles offset on *y*-axis for clarity.

vesicle, which could be a result of insufficient contrast between the Fe(III)−M_E bilayer and the space between bilayers.

A sample containing the Zn(II)-induced particles (1.4 mM Fe(III)−M_E, 3.5 mM Zn(II)) was also imaged by freeze-fracture TEM (FF-TEM).[26] A very small number (ca. five) of globular objects (∼100 nm diameter) were observed in FF-TEM images (data not shown); however, the globular objects were too sparse for us to determine if they were representative of the sample.

Zinc(II)-Induced Phase Transition with Fe(III)−Marinobactin B and D. *Dynamic Light Scattering.* Marinobactins B and D have the same headgroup and coordination geometry to Fe(III) as Fe(III)−M_E but differ in the identity of the fatty acid tails (Figure 1). Fe(III)−M_D is a ca. 1:3 mixture of Fe(III)−M_{D1} and Fe(III)−M_{D2}, which have cis double bonds in the ω-7 and ω-9 positions of the fatty acid tail, respectively (Figure 1). The hydrocarbon tail of Fe(III)−M_B also contains a cis double bond in the ω-7 position but is shorter than the fatty acid tails of Fe(III)−M_D and Fe(III)−M_E by two methylene groups (Figure 1). Adding 0.5 or 3.5 mM Zn(II) to Fe(III)−M_B or Fe(III)−M_D, respectively, (1.4 mM Fe(III)−marinobactin, pD 6.0, 37 °C) produces a milky, turbid solution similar to that observed with Fe(III)−M_E in the presence of 3.5 mM Zn(II) at 37 °C. DLS measurements reveal that the Zn(II)-induced particles of Fe(III)−M_B and Fe(III)−M_D were relatively monodisperse in size (polydispersity <0.25) for a given sample preparation, although the average diameter varied considerably between sample preparations (i.e., 1.4 mM Fe(III)−M_D with 3.5 mM Zn(II) at pD 6.0 and 37 °C). Specifically, the average diameter of the Zn(II) particles ranged from 170 to 250 nm for Fe(III)−M_B and from 150 to 220 nm Fe(III)−M_D.

Small-Angle Neutron Scattering. SANS profiles of the Zn(II)-induced aggregates formed by Fe(III)−M_B and Fe(III)−M_D (at 25 °C, Figure 5) are similar to SANS profiles of the Zn(II)-induced particles formed by Fe(III)−M_E (at 37 °C, Figure 3) and display a Bragg peak at $Q \approx 0.11-0.12$ Å^{-1}. The Bragg peak position is shifted to slightly higher Q (smaller interlamellar repeat distance) in the case of Fe(III)−M_B (Figure 5 inset) relative to Fe(III)−marinobactins with longer fatty acid tails (e.g., Fe(III)−M_D (Figure 5 inset) and Fe(III)−M_E (Figure 3 inset)). In the case of Fe(III)−M_D, the SANS profile displays a shoulder at $Q \approx 0.005$ Å^{-1} that could be indicative of a relatively monodisperse population of particles such as multilamellar vesicles. The fitted vesicle parameters (Table 2)[27] for the Zn(II)-induced Fe(III)−M_B and Fe(III)−M_D particles are similar to those obtained for Fe(III)−M_E with 3.5 mM Zn(II) (Table 1), although notably, the vesicle core polydispersity is lower in the case of Fe(III)−M_D.[28]

Cd(II)- and La(III)-Induced Phase Transitions with Fe(III)−M_E. *Small-Angle Neutron Scattering*. SANS profiles of the Cd(II)- and La(III)-induced particles exhibited a similar Bragg peak at $Q_B \approx 0.11$ Å^{-1} as SANS profiles of the Zn(II)-induced particles (Figure 6), suggesting that all three cations induce the formation of aggregates with a periodic microstructure of ∼5.6−5.7 nm. The intensity of the low-Q scattering from the La(III)-induced particles extends to higher-Q values than for the Cd(II) or Zn(II)-induced particles, suggesting that La(III) induces Fe(III)−M_E to form aggregates of a smaller size than Cd(II) or Zn(II). Fitting SANS profiles of the Cd(II)-induced phase to the multilamellar vesicle scattering model produced similar qualitative results as were obtained in the case of the Zn(II)-induced phase (Table 1). Specifically, the fitted vesicle core radius was a small fraction of the overall vesicle diameter (ca. 18%), suggesting that the vesicles have bilayers extending nearly to the center of the particle. The best fit to SANS profiles for the La(III)-induced phase (Figure 6, fit not shown) was obtained using a mixture of two vesicle populations with two and three bilayers. However, the quality of fit in the case of the La(III)-induced phase was much poorer ($\chi^2 = 34.1$) than that obtained with the Cd(II)- or Zn(II)-induced particles (Table 1), suggesting that the multilamellar SANS model may be inappropriate to describe SANS profiles of the La(III)-induced phase.

Dynamic Light Scattering. The addition of 3.5 mM Cd(II) or 0.5 mM La(III) to 1.4 mM Fe(III)−M_E solutions and equilibrating for 72 h at 37 °C (pD 6.0) produced a turbid solution similar to that obtained upon 3.5 mM Zn(II) addition to 1.4 mM Fe(III)−M_E under the same conditions. DLS measurements show that Cd(II) containing Fe(III)−M_E solutions consisted of a relatively monodisperse population (polydispersity <0.2) of particles with an average fitted diameter that varied between ca. 100 and 190 nm each time a particular sample (e.g., 1.4 mM Fe(III)−M_E with 3.5 mM Cd(II) at pD 6.0 and 37 °C) was prepared. DLS measurements of La(III)-containing Fe(III)−M_E solutions yielded a correlation function that was inconsistent with a monodisperse

Table 2. Micelle and Vesicle Parameters for Fe(III)−M_B and Fe(III)−M_D with Zn(II)[a]

SANS fit parameters		Fe(III)−M_B, 0.5 mM Zn(II)	Fe(III)−M_D, 3.5 mM Zn(II)
micelle	volume fraction (±0.001%)	0.009	0.021
	diameter (±0.1 nm)[b]	3.0	4.3
	polydispersity (±0.01)[b]	0.25	0.26
multilamellar vesicle	diameter	199	225
	core diameter (±0.2 nm)	32.4	34.1
	core polydispersity (±0.01)	1.00	0.55
	bilayer thickness[b]	2.6	2.8
	interbilayer thickness[b]	2.6	2.8
vesicle population no. 1	volume fraction (±0.001%)	0.047	0.066
	no. of bilayers	16	17
	χ^2	7.6	7.2

[a] Fe(III)−marinobactin (1.4 mM), pD 6.0, 25 °C. [b] Micelle diameter and polydispersity as well as vesicle bilayer thickness and interbilayer thickness are constrained as described in the text.

(26) (a) Zasadzinski, J. A.; Bailey, S. M. *J. Electron Microsc. Tech.* **1989**, *13*, 309−334. (b) Keller, S. L.; Boltenhagen, P.; Pine, D. J.; Zasadzinski, J. A. *Phys. Rev. Lett.* **1998**, *80*, 2725−2728. (c) Spector, M. S.; Naranjo, E.; Chiruvolu, S.; Zasadzinski, J. A. *Phys. Rev. Lett.* **1994**, *73*, 2867−2870.

(27) The multilamellar vesicle model was fit to the Fe(III)−M_B and Fe(III)−M_D SANS profiles using the same procedure outlined for Fe(III)−M_E, except that the Fe(III)−M_D micelle diameter and polydispersity were obtained from SANS measurements of Fe(III)−M_D micelles at 10 °C (Figure S-3 and Table S-3 in Supporting information). The Fe(III)−M_B micelles were not concentrated enough (at 10, 25, or 37 °C) to get a reliable measurement of their parameters; therefore, the Fe(III)-M_B micelle diameter and polydispersity were arbitrarily fixed at 3 nm and 0.25, respectively. Using different parameters for the Fe(III)−M_B micelles did not significantly change the other fitted parameters or the quality of fit (i.e., c2).

(28) The simulated SANS profile from the multilamellar vesicle model sometimes exhibits "spikes" in Q regions where data obtained at two different sample-to-detector-distances overlap (e.g., 2 and 13 m sample-to-detector distances). The spikes occur because the SANS model was smeared with instrumental resolution parameters and those parameters are not the same at different sample-to-detector-distances. Smearing the SANS model with different instrumental resolution parameters can result in slightly different calculated values for the simulated SANS intensity at the same Q value and can cause a spike in the simulated profile. This phenomena is evident in the fit to the SANS profiles of the Zn(II)-induced particles formed from Fe(III)−M_B and Fe(III)−M_D (Figure 5) at $Q \approx 0.008$ Å^{-1}.

population of particles, which suggests that the La(III)-induced aggregates are more polydisperse than the Zn(II)- and Cd(II)-induced particles.

Discussion

Zn(II) induces a change in aggregate morphology in which Fe(III)−M_E micelles are converted to large spherical particles (∼100−200 nm diameter) at 37 °C. SANS profiles of the Zn-(II)-induced particles are consistent with multilamellar vesicles (Figure 3). The Bragg peak at $Q_B \approx 0.11$ Å^{-1} is suggestive of liposomes with an interlamellar repeat distance of $2\pi/Q_B \approx 5.6$ nm. Fitting SANS data to the multilamellar vesicle model indicates that the solvent-filled core makes up a small fraction (<1%) of the overall vesicle volume, which is consistent with the fact that the solvent-filled core is not visible in cryo-TEM images of the Zn(II)-induced particles (Figure 4). Interlamellar spacing was not discernible in the cryo-TEM images (Figure 4), which could result from insufficient contrast between the vesicle bilayer and the space between bilayers. In fact, if the space between bilayers was occupied by the surfactant headgroup or a sufficient concentration of Zn(II), then the interlamellar spacing would not be resolved. Thus, the SANS and cryo-TEM data suggests that Zn(II) induces Fe(III)−M_E to form multilamellar vesicles characterized by a small solvent-filled core volume relative to the overall vesicle volume.[29]

The metal-induced phase behavior can be rationalized in terms of the coordination chemistry of carboxylic acids with the metals investigated. Cd(II), Zn(II), and La(III) form 2:1 ligand/metal coordination complexes with carboxylic acids, such as acetic acid ($\beta_2 = 4.8 \times 10^2$, 1.2×10^2, 1.8×10^2, respectively, at 0.01 M ionic strength), whereas Ca^{2+} and Ba^{2+} are reported to coordinate only a single acetate in aqueous solution ($K_1 = 9.5$ and 13.3, respectively).[30] The ability of Cd(II), Zn(II), and La-(III) to coordinate two acetate ligands suggests that these metal cations may drive the phase transition by bridging the terminal carboxylate moiety of two or more Fe(III)−M_E headgroups (e.g., forming ≥2:1 Fe(III)−M_E/Zn(II) complexes) and pulling them closer together. Bridging two headgroups with a metal cation effectively produces a cylindrical composite surfactant molecule with two alkyl tails that would likely favor a vesicular arrangement (Scheme 1) relative to a cone-shaped, monocephalic surfactant that would be thermodynamically predisposed to form micelles.[36] Thus, Cd(II), Zn(II), and La(III) may induce the formation of multilamellar vesicles by bridging multiple Fe(III)−M_E headgroups. Solvent-ordering effects (e.g., Hofmeister effects),[31,32] could also be important in the cation (e.g., Zn(II), Cd(II), or La(III)) stabilization of the liposome.

The surface concentration of metal-bridged headgroups (i.e., Zn(II)-bridged headgroups) on a given bilayer in a Zn(II)-induced multilamellar vesicle may be lower for bilayers near the vesicle core versus the bilayers at or near the perimeter. Decreasing the surface concentration of metal-bridged headgroups (and therefore increasing the surface concentration of individual unbridged headgroups) is expected allow a greater membrane curvature assuming that metal-bridged Fe(III)−M_E molecules are more rodlike in shape relative to individual Fe(III)−M_E molecules. Therefore, varying the surface concentration of metal-bridged headgroups in this manner could allow for the greater membrane curvatures of bilayers near the core of the liposome relative to the perimeter.[33]

If the metal cation (e.g., Zn(II), Cd(II), and La(III)) bridges more than one Fe(III)−marinobactin headgroup in the metal-induced particles, then the ratio of bridging metal cation to Fe-(III)−marinobactin in the metal-induced aggregates should be less than 1. Therefore, one might expect the metal-induced particles to form when less than1 equiv of metal cation is added to a solution containing 1 equiv of Fe(III)−marinobactin. Indeed, Zn(II)-induced particles form when the Zn(II)/Fe(III)−marinobactin ratio is as low as 0.35 in the case of Fe(III)−M_B (M_B has a C_{14}, unsaturated fatty acid tail; Figure 1). However, Fe(III)−M_E, which has a longer fatty acid tail (i.e., C_{16}, saturated, Figure 1) than Fe(III)−M_B, requires a Zn(II)/Fe(III)−marinobactin ratio of greater than 1.3 (Figure 3) before a phase change is observed; the concentration of Fe(III)−marinobactin is 1.4 mM in both cases. At this point, it is not clear why Fe(III)−M_E requires more than 1 equiv of Zn(II) to undergo the Zn(II)-induced transition; however, ratios of metal cation to surfactant that are greater than 1 are also required for metal-induced phase changes by other anionic surfactants. For instance, a Ca^{2+} to surfactant ratio of ca. 2:1 induces the lamellar to reverse hexagonal phase transition of cardiolipin as well as 1,2-dioleioylphosphatidic acid.[7,34]

It is interesting that the Zn(II)-induced-transition with Fe-(III)−M_E occurred only above 25 °C because assembling many small micelles into a large ∼100 nm diameter aggregate is expected to be entropically disfavored. An increase in membrane fluidity at higher temperatures has been used to explain the elevated temperature requirement for Ca(II)-induced vesicle fusion in phospholipid systems.[35] A similar mechanism may explain the phase behavior of Fe(III)−marinobactin in which an elevated temperature is required to increase the fluidity of the surfactant's fatty acid tail so that micelles are able to fuse into a larger, more energetically favorable aggregate. This hypothesis is corroborated by the fact that Fe(III)−M_B and Fe(III)−M_D undergo the Zn(II)-induced phase transition at lower temperatures (e.g., 25 °C and below; Figure S-3 and Table S-3 in Supporting Information) than Fe(III)−M_E because Fe(III)−M_B and Fe(III)−M_D have unsaturated hydrocarbon tails (C_{14} and C_{16}, respectively, Figure 1) and are expected to have lower melting temperatures than Fe(III)−M_E, which contains a saturated C_{16} lipid tail.

Zn(II), Cd(II), and La(III) effect a phase change in Fe(III)−M_E that is similar to the Fe(III)-induced micelle-to-vesicle transition reported previously.[11] The effect that these multivalent cations have on the phase behavior of Fe(III)−M_E has opened up new questions regarding the role that these and other cations may play in iron uptake by the source bacterium. To date, a variety of marine bacteria have been shown to produce amphiphilic siderophores with anionic peptidic headgroups that may

(29) Alternatively, the Zn(II)-induced particles could be a non-lamellar dispersed phase (e.g., hexosomes: Yaghmur, A.; de Campo, L.; Sagalowicz, L.; Leser, M. E.; Glatter, O. *Langmuir* **2005**, 21, 569−577), which can have the appearance of solid spheres by cryo-TEM as well as give rise to a Bragg peak (Figure 3). However, given that Fe(III)−M_E forms multilamellar vesicles in the presence of excess Fe(III),[10,11] it seems reasonable that Fe(III)−M_E also forms multilamellar vesicles in the presence of Zn(II).

(30) Martell, A. E.; Sillen, L. G. *Stability Constants of Metal Ion Complexes*; The Chemical Society, Burlington House: London, 1971; Supplement No. 1, pp 250−256.

(31) Collins, K. D. *Methods* **2004**, 34, 300−311.

(32) Cacace, M. G.; Landau, E. M.; Ramsden, J. J. *Q. Rev. Biophys.* **1997**, *30*, 241−277.

(33) A lower surface concentration of metal cations for bilayers near a liposomes core vs the perimeter would suggest that the net charge of bilayers near the core would be different from the net charge of bilayers near the perimeter. Such a separation of charge in a liposome would be energetically unfavorable; however, a greater surface concentration of metal cations on a bilayer could also cause greater ionization of neighboring carboxylic acids in the same bilayer (i.e., could lower the pK_a of neighboring carboxylic acids). Thus, the bilayer charge could be the same for bilayers near the liposomal core vs the perimeter, and the vesicle core would be electroneutral with its perimeter.

(34) Verkleij, A. J.; de Maagd, R.; Leunissen-Bijvelt, J.; de Kruijff, B. *Biochim. Biophys. Acta* **1982**, *684*, 225−262.

(35) Papahadjopoulos, D.; Vail, W. J.; Pangborn, W. A.; Poste, G. *Biochim. Biophys. Acta* **1976**, *448*, 265−283.

(36) Israelachvili, J. N.; Mitchell, D. J.; Ninham, B. W. *J. Chem. Soc., Faraday Trans. 2* **1976**, *72*, 1525−1568.

also participate in metal-dependent phase behavior similar to that of the marinobactins. Future studies with the marinobactins and other amphiphilic siderophores will focus on elucidating the metal coordination environment of the cross-linking metal ion (e.g., with X-ray absorption spectroscopy) to understand better how the interplay between metal-coordination chemistry and surfactant self-assembly governs the phase behavior of this biologically and technologically relevant system.

Acknowledgment. We gratefully acknowledge support from NIH GM38130 (AB), NSF NIRT grant CHE0103516 (AB), and NSF EMSI grant CHE0221978 (AB) and U.S. Department of Energy contract W-7405-ENG-36 with the University of California (R.P.). We thank R. van Zanten, P. Stenger, and J. Zasadzinski for assistance with cryo-TEM and FF-TEM on equipment funded by NSF-0436124, S. Kline (NIST Center for Neutron Research) for advice on developing the SANS model, and J. Barker (NIST Center for Neutron Research) for performing specific SANS measurements. Certain commercial equipment, instruments, and materials are identified in this article to foster understanding. Such identification does not imply a recommendation or endorsement by the National Institute of Standards and Technology nor does it imply that the materials or equipment identified are necessarily the best available for the purpose. This work is also based upon activities supported in part by the National Science Foundation under agreement no. DMR-0454672.

Supporting Information Available: Dependence of micelle size on the metal cation. Comparison of the fit of two different multilamellar vesicle SANS models. Temperature dependence of the Zn(II)-induced transition. This material is available free of charge via the Internet at http://pubs.acs.org.

LA700671P